Remote Sensing of Environment 163 (2015) 240–252

Contents lists available at ScienceDirect

Remote Sensing of Environment

journal homepage: www.elsevier.com/locate/rse

Bering Sea optical and biological properties from MODIS

Puneeta Naik [a,b], Menghua Wang [a,*], Eurico J. D'Sa [c], Calvin W. Mordy [d,e]

[a] NOAA National Environmental Satellite, Data, and Information Service, Center for Satellite Applications and Research, E/RA3, 5830 University Research Court, College Park, MD 20740, USA
[b] CIRA, Colorado State University, Fort Collins, CO 80523, USA
[c] Department of Oceanography and Coastal Sciences, Louisiana State University, Baton Rouge, LA 70803, USA
[d] Joint Institute for the Study of the Atmosphere and Ocean, Box 355672, University of Washington, Seattle, WA 98105-5672, USA
[e] Pacific Marine Environmental Laboratory, NOAA, 7600 Sand Point Way, NE, Seattle WA 98115, USA

ARTICLE INFO

Article history:
Received 28 June 2014
Received in revised form 18 March 2015
Accepted 22 March 2015
Available online 23 April 2015

Keywords:
Bering Sea
Ocean color remote sensing
Chlorophyll-a algorithm
Water optical and biological properties

ABSTRACT

The Bering Sea is characterized by unique bio-optical properties, which cause unsatisfactory performance of global ocean color algorithms for retrieval of chlorophyll-a (Chl-a). This study evaluates the normalized water-leaving radiance $nL_w(\lambda)$ and Chl-a in the eastern Bering Sea that are derived from the Moderate Resolution Imaging Spectroradiometer (MODIS) on the satellite Aqua by comparing them to in situ data. MODIS-Aqua ocean color products were derived using the NOAA Multi-Sensor Level-1 to Level-2 (MSL12) ocean color data processing system. The MODIS-derived $nL_w(\lambda)$ showed good agreement with in situ-measured $nL_w(\lambda)$. The mean ratios between them for wavelengths 412, 443, 488, and 551 nm ranged from 1.097 to 1.280, with reasonably accurate blue-green radiance ratios in $nL_w(\lambda)$ that were used as input for deriving Chl-a. However, compared to in situ data, existing global and regional Chl-a algorithms either overestimate or underestimate Chl-a in the eastern Bering Sea. Therefore, we propose a new algorithm for estimating Chl-a using a blended approach that was tested and applied to MODIS-Aqua images. The histogram distributions of MODIS-Aqua-derived and in situ-measured Chl-a data show that Chl-a data derived using the new algorithm agree reasonably well to in situ measurements. Annual, seasonal, and monthly composite $nL_w(\lambda)$ and Chl-a images are produced for the period of 2003 to 2013 in order to interpret the long-term spatial and temporal patterns of $nL_w(\lambda)$ and Chl-a. The $nL_w(\lambda)$ spectra show strong spectral dependence on seasonal variability with distinct spatial patterns. Although strong seasonal and interannual variability has been observed in Chl-a, there is no apparent trend of either increase or decrease in phytoplankton biomass associated with variability in the physical environment for the 11 years of the study period.

Published by Elsevier Inc.

1. Introduction

The Bering Sea has been recognized as one of the most productive continental shelves in the world, supporting half of the US fishery catch (Overland & Stabeno, 2004; Sigler et al., 2010). High rates of primary production driven by seasonal sea ice, stratification, and light conditions sustain the abundant benthic biomass and higher trophic levels (Grebmeier & Cooper, 1995; McRoy, Hansell, Springer, Walsh, & Whitledge, 1987; Stabeno, Hunt, Napp, & Schumacher, 2006). In recent years, the Bering Sea is rapidly restructuring its marine environment (Grebmeier et al., 2006; Hunt et al., 2002; Overland & Stabeno, 2004; Walsh & McRoy, 1986). Intensive scientific studies have been conducted in the Bering Sea in recent decades due to its economic importance and its rich ecosystem that is rapidly changing (McRoy, Hood, Coachman, Walsh, & Goering, 1986), e.g., Bering Ecosystem Study—Bering Sea Integrated Ecosystem Research Program (BEST—BSIERP) (http://bsierp.nprb.org). The Bering Sea is characterized by strong seasonality with a physical and biological structure shaped mainly by sea ice concentration (Overland & Stabeno, 2004; Stabeno, Schumacher, & Ohtani, 1999). Due to the strong seasonality and associated response of primary producers, it is challenging to monitor and characterize changes in the Bering Sea from in situ measurements as well as satellite observations. Most of the research in the Bering Sea has focused on climatic fluctuations and its effects on the physical and biological regimes of the Bering Sea (Mathis et al., 2010; Overland & Stabeno, 2004; Sigler et al., 2010; Stabeno et al., 2012b). However, some of these impacts still remain ambiguous. Part of this ambiguity can be ascribed to the fact that even numerous individual ship-borne measurements integrated over large spatial and temporal scales do not always capture the diversity and dynamicity of the Bering Sea. In this context, satellite remote sensing can be an invaluable resource for understanding and monitoring the rapid changes in the Bering Sea at spatial and temporal scales unachievable by traditional shipboard in situ observations. Ocean color measurements from satellites have served as an important tool for assessing changes in primary productivity in response to climate (Aiken, Moore, & Hotligan, 1992; Behrenfeld et al., 2001, 2006). However, satellite Chl-a estimates generally used as inputs to primary productivity

* Corresponding author.
E-mail address: Menghua.Wang@noaa.gov (M. Wang).

http://dx.doi.org/10.1016/j.rse.2015.03.020
0034-4257/Published by Elsevier Inc.

algorithms (Behrenfeld & Falkowski, 1997; Son, Wang, & Harding, 2014) are known to lack accuracy at high latitudes (Cota, Wang, & Comiso, 2004; Matsuoka, Huot, Shimada, Saitoh, & Babin, 2007; Mitchell & Holm-Hansen, 1991; Naik, D'Sa, Gomes, Goés, & Mouw, 2013; Schallenberg, Lewis, Kelley, & Cullen, 2008). One of the major reasons is that the current ocean color Chl-a algorithms were developed using measurements primarily from lower latitudes (Bailey & Werdell, 2006; Werdell & Bailey, 2005).

Due to the distinctive bio-optical environment of the Bering Sea, the performance of global Chl-a algorithms (O'Reilly et al., 1998, 2000) is unsatisfactory (Naik et al., 2013). More specifically, the elevated levels of colored dissolved organic matter (CDOM) absorption results in overestimation, while highly packaged pigments associated with large cells contribute to underestimation of Chl-a retrieved using the global empirical ocean color algorithms at lower and higher Chl-a concentrations (Naik et al., 2013), respectively. In addition, the weak correlation between Chl-a and detrital plus CDOM absorption, which together dominate total light absorption at blue wavelengths, cause the poor performance of the global empirical ocean color algorithms. Regionally tuned algorithms should capture some of these distinctive bio-optical properties and improve the accuracy of Chl-a retrievals, thereby enhancing our capability to detect phytoplankton fluctuations associated with climate change in the Bering Sea.

In this paper, using long-term measurements from the Moderate Resolution Imaging Spectroradiometer (MODIS) on the satellite Aqua (Salomonson, Barnes, Maymon, Montgomery, & Ostrow, 1989), we evaluate the performance of global and regional Chl-a algorithms, and propose a new blended Chl-a algorithm for the eastern Bering Sea. In addition, the performance of MODIS-Aqua-derived normalized water-leaving radiance spectra $nL_w(\lambda)$ (Gordon, 2005; IOCCG, 2010; Morel & Gentili, 1996; Wang, 2006a), which are input to Chl-a algorithms, are evaluated and its long-term spatial and temporal patterns are analyzed. MODIS-Aqua ocean color products are derived using the NOAA Multi-Sensor Level-1 to Level-2 (MSL12) ocean color data processing system, which will be briefly described and discussed. The new blended Chl-a algorithm is applied to MODIS-Aqua data to characterize seasonal and interannual variability of Chl-a in relation to climatic variability in the eastern Bering Sea.

2. Study area

The Bering Sea is a semi-enclosed sub-arctic sea linked to the Arctic Ocean through the Bering Strait and to the North Pacific through the Aleutian Islands (Fig. 1). The Bering Sea, like other sub-arctic marginal seas, is characterized by seasonal ice coverage and high biological productivity (Schumacher & Stabeno, 1998; Stabeno et al., 1999). The eastern Bering Sea shelf has a dynamic physical environment that is mainly controlled by seasonal sea ice cover. During winter the water column is well mixed. In summer the shelf can be divided into three distinct domains across the shelf, the inner domain, the middle domain, and the outer domain (Fig. 1), which is based on two distinct oceanographic fronts, i.e., the inner front and the middle front (Coachman, 1986; Kachel et al., 2002). Overlying the ~50 m isobath, the inner front separates the inner domain from the middle domain, while the middle front is a broad transitional zone between approximately the 80 and 100 m isobath that separates the middle domain from the outer domain (Fig. 1). Each of these domains has characteristics in the physical, biological, and biogeochemical environment (Lomas et al., 2012; Mathis et al., 2010; Moran et al., 2012). The eastern Bering shelf can be further divided along the shelf into northern and southern regions at ~60°N (Stabeno et al., 2012a). The broad shelf (depth < 200 m) is separated from the deep basin (depth > 200 m) by a steep continental slope.

Sea ice is the main governing factor that controls the physical and chemical environment of the eastern Bering Sea shelf (Stabeno et al.,

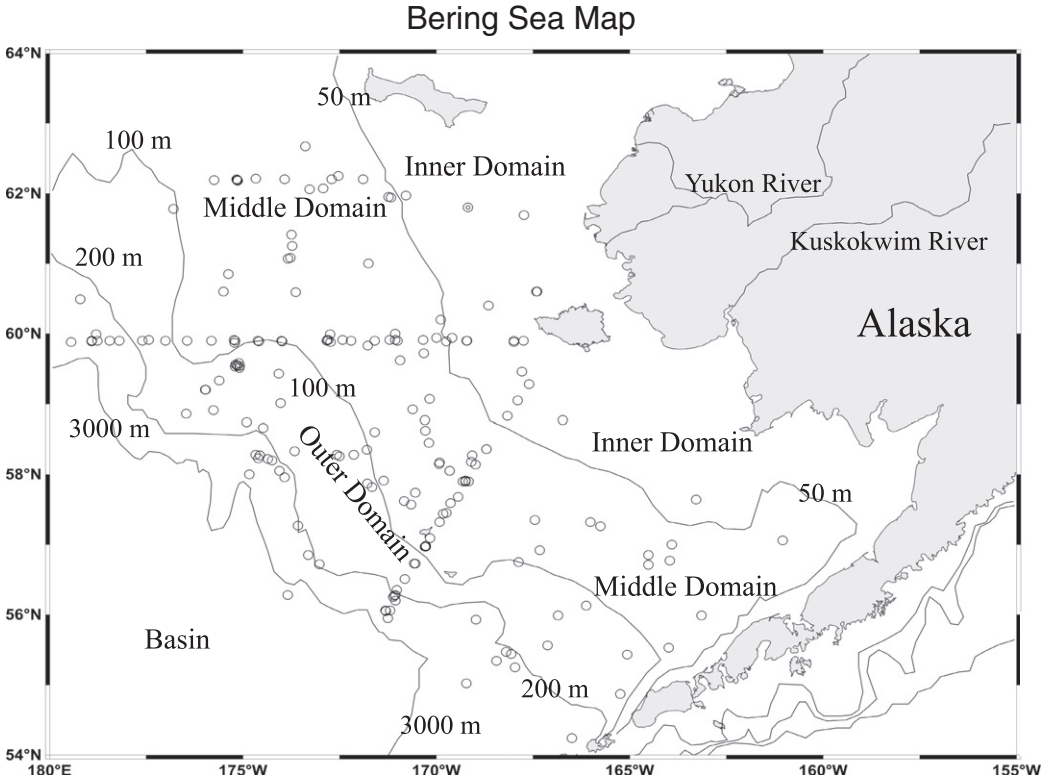

Fig. 1. Map of the eastern Bering Sea. Locations of the in situ radiometric and Chl-a measurements are shown in black circles. The labeled solid lines indicate the 50, 100, 200, and 3000 m isobaths that divide the shelf into the inner domain, middle domain, outer domain, and basin region, respectively.

1999). Sea ice forms in latent heat polynyas off the coasts and lee side of islands and is gradually driven southward by prevailing north-northeasterly winds (Niebauer, Bond, Yakunin, & Plotnikov, 1999). The ice edge melts when it comes in contact with warmer water, thus the melting sea at the southern edge assists in further ice progress. However, southerly transport of sea ice does not extend beyond the shelf break as it encounters the basin waters that contain large reservoirs of heat content (Niebauer et al., 1999). An important feature of the eastern Bering Sea shelf is the development of the cold pool in response to sea ice formation. This cold pool develops in the previous winter and is located in the central part of the shelf where it persists throughout summer constrained below the seasonal thermocline (Hunt et al., 2002; Kachel et al., 2002; Stabeno, Bond, Kachel, Salo, & Schumacher, 2001). The cold pool is defined as the region where the bottom water temperatures are below 2 °C (Hunt et al., 2002; Stabeno et al., 2001). It serves as an important migration barrier for subarctic fish species such as the commercially important walleye pollock (Kotwicki, Buckley, Honkalehto, & Walters, 2005; Mueter & Litzow, 2008), and it significantly affects the benthic predators (Grebmeier et al., 2006). The cold pool is subjected to significant interannual variability closely tied to atmospheric, oceanic, and sea ice conditions during the previous winter (Stabeno et al., 2001) and is thought to move northward in response to sea ice loss (Mueter & Litzow, 2008).

The primary productivity in the eastern Bering Shelf is characterized by strong temporal and spatial variability with localized regions of high productivity (McRoy et al., 1987; Niebauer, Alexander, & Cooney, 1981; Sambrotto, Niebauer, Goering, & Iverson, 1986; Springer & McRoy, 1993; Springer, McRoy, & Flint, 1996). The eastern Bering shelf waters are generally regarded as nitrogen limited, while the deep basin is considered as a high nutrient low chlorophyll (HNLC) region (Leblanc et al., 2005). The confluence of these nutrient conditions, together with physical processes at the shelf break, support high levels of primary production at the shelf break region also known as the 'green belt' (Springer et al., 1996). The spring phytoplankton bloom, which represents the bulk of the annual primary production, develops in the eastern shelf and lasts until the nutrients in the shallow regions are exhausted (Sigler et al., 2010; Sigler, Stabeno, Eisner, Napp, & Mueter, 2014). Sea ice and its retreat appear to control the dynamics of the spring phytoplankton bloom and its subsequent transfer of energy to high trophic levels (Coyle et al., 2011; Hunt & Stabeno, 2002; Hunt et al., 2002, 2011; Stabeno et al., 2001). Late sea ice retreat (April–May) during cold years fosters an ice edge bloom, and much of this production is exported to the benthos (Overland & Stabeno, 2004). On the other hand, when the sea ice retreats in early March, the bloom does not develop until May or June, and most of the energy from the bloom is restricted to the pelagic environment (Hunt & Stabeno, 2002; Stabeno et al., 2001). Thus, the timing of sea ice melting impacts an early versus late phytoplankton bloom, and subsequently the type of ecosystem being created, i.e., benthic or pelagic, which has a cascading effect on higher trophic levels (Coyle et al., 2011; Hunt et al., 2002, 2011; Overland & Stabeno, 2004).

3. Data and methods

3.1. NOAA-MSL12 ocean color data processing system

The NOAA-MSL12 ocean color data processing system has been used to process and generate MODIS-Aqua ocean color products. MSL12 was developed for a consistent and common ocean color data processing system to produce ocean color data from multiple ocean color satellite sensors (Wang, 1999; Wang & Franz, 2000; Wang, Isaacman, Franz, & McClain, 2002). Specifically, NOAA-MSL12 is based on the Sea-viewing Wide Field-of-View Sensor (SeaWiFS) Data Analysis System (SeaDAS) version 4.6, which uses the Gordon and Wang (1994) standard near-infrared (NIR) atmospheric correction algorithm (Gordon & Wang, 1994). However, it should be noted that the NOAA-MSL12 has been modified and improved to include: (1) the shortwave infrared (SWIR)-based and NIR-SWIR combined ocean color data processing (Wang, 2007; Wang & Shi, 2007; Wang, Son, & Shi, 2009); (2) improved aerosol lookup tables (including polarization effect) and more accurate Rayleigh radiance (Wang, 2005, 2006a,b); (3) algorithms for detecting absorbing aerosols and turbid waters (Shi & Wang, 2007); (4) improved cloud masking for coastal and inland waters (Wang & Shi, 2006); (5) implementation of an ice-detection algorithm for global and regional ocean color data processing (Wang & Shi, 2009), and other improvements, e.g., identification of stray light and cloud shadow contaminations (Jiang & Wang, 2013), an approach to improve the performance of MODIS SWIR bands (Wang & Shi, 2012). Also, for the NOAA operational ocean color data processing (near-real time), ancillary data (the total column ozone amount, sea surface wind speed, atmospheric pressure, and total column water-vapor amount) from the Global Forecast System (GFS) model are used (Ramachandran & Wang, 2011). The NOAA-MSL12 is also capable of deriving ocean color products from the Visible Infrared Imaging Radiometer Suite (VIIRS) onboard the Suomi National Polar-orbiting Partnership (SNPP) and has been routinely producing VIIRS global ocean color products since VIIRS launch on October 28, 2011 (Wang et al., 2013b).

In this study, we use the NIR-SWIR combined atmospheric correction algorithm (Wang & Shi, 2007; Wang et al., 2009) in the NOAA-MSL12 ocean color data processing system for generating ocean color products from MODIS-Aqua measurements in the Bering Sea.

3.2. In situ data

A large database of in situ Chl-a data was obtained from the BEST data archive, which is an NSF funded project in the Bering Sea (http://www.nprb.org/bering-sea-project). A total of 1328 samples of Chl-a recorded from a depth less than 3 m were obtained from the BEST data archive (https://www.eol.ucar.edu/projects/best/). The in situ Chl-a data were collected from March through July from 2007–2010 and data ranged from ~0.04–40 mg m^{-3}.

In situ normalized water-leaving radiance $nL_w(\lambda)$ data in the Bering Sea were obtained from the SeaWiFS Bio-optical Archive and Storage System (SeaBASS) (http://seabass.gsfc.nasa.gov/) (Werdell et al., 2003) and a research cruise on the US Coast Guard Cutter (USCGC) *Healy* in July 2008 in the region. The details on the in situ $nL_w(\lambda)$ data processing are described in Naik et al. (2013). Our analysis of the radiometric data is restricted for $nL_w(\lambda)$ at wavelengths of 412, 443, 488, and 555 nm as there are fewer than 10 data points at other wavelengths. In addition, Chl-a data corresponding to the existing SeaBASS $nL_w(\lambda)$ data were also obtained from SeaBASS.

3.3. MODIS-Aqua data

MODIS-Aqua Level-1B data (Collection 6) were obtained from the NASA MODIS Adaptive Processing System (MODAPS) website (http://ladsweb.nascom.nasa.gov). These Level-1B data were processed to ocean color Level-2 products using NOAA-MSL12 with the NIR-SWIR atmospheric correction algorithm (Wang, 2007; Wang & Shi, 2007; Wang et al., 2009). Daily sea ice mask based on sea ice data obtained from NASA was applied to daily Level-2 images. In addition, the Level-2 MODIS-Aqua ocean color data products were mapped to 1-km spatial resolution and processed to generate daily, monthly, seasonal, and annual composites. We defined the seasons in the region as follows: March, April, and May are considered as spring, June, July, and August as summer, September, October, and November as fall, and December, January, and February as winter.

For matchups of satellite-derived and in situ-measured ocean color products, we applied a procedure similar to Wang et al. (2009). The procedure was designed to remove any spatial heterogeneity owing to patchiness in waters from retrieved pixels. A 5 × 5 pixel box centered at the in situ measurement location was used to extract MODIS-Aqua

Level-2 ocean color products. If the number of pixels in the 5 × 5 box exceeded 13 (>50% of pixels), then the matchup pair between MODIS-Aqua and in situ data was included for further analysis. In addition, only those pixels within 1.5 standard deviation (STD) of the mean in the 5 × 5 box were included to recalculate the revised mean (Wang et al., 2009). For the matchup analyses, several time difference windows between MODIS-Aqua-derived and in situ-measured variables were analyzed to determine the optimum temporal resolution (discussed later in Section 4.2). As the Bering Sea has persistent cloud cover throughout the year, the standard recommendation of ±3 hours (Bailey & Werdell, 2006) was too short to get an adequate number of valid matchup pairs for a statistically significant analysis. A set of masks (Wang et al., 2009) corresponding to high solar-zenith angle, high sensor-zenith angle, sun glint, cloud/ice, and land were applied to both individual granules for matchup analysis as well as to composite images generated from MODIS-Aqua Level-2 data. In particular, a new stray light flag (Jiang & Wang, 2013) was applied and satellite data noise was significantly reduced.

3.4. Sea ice extent, sea surface temperature, and wind speed

Sea ice extent data (2003–2012) were obtained from the National Snow and Ice data center (https://nsidc.org/). These data were derived from the Nimbus-7 Scanning Multichannel Microwave Radiometer (SMMR) and the Defense Meteorological Satellite Program (DMSP) Special Sensor Microwave/Imagers (SSM/Is) using the NASA team algorithm developed by the Oceans and Ice Branch, Laboratory for Hydrospheric Processes at NASA Goddard Space Flight Center (GSFC). These data produced by the NASA team have a one-year latency period.

In addition, the wind speed data were obtained from the National Centers for Environmental Prediction/National Center for Atmospheric Research (NCEP/NCAR) reanalysis project (http://www.esrl.noaa.gov/psd/), and MODIS-Aqua Level-2 sea surface temperature (SST) data were obtained from NASA Ocean Biology Processing Group (OBPG) (http://oceancolor.gsfc.nasa.gov).

3.5. Chl-a algorithms

We evaluate the accuracy of three satellite ocean color empirical algorithms to retrieve Chl-a, i.e., the MODIS-Aqua standard algorithm OC3M (O'Reilly et al., 1998, 2000), an algorithm tuned for the Arctic Ocean OC4L (Cota et al., 2004), and an algorithm tuned to the Bering Sea, BS-OC (Naik et al., 2013). These empirical algorithms calculate Chl-a from band ratios of normalized water-leaving reflectance $\rho_{wN}(\lambda)$ (Gordon & Wang, 1994), defined as $\rho_{wN}(\lambda) = \pi \cdot nL_w(\lambda)/F_0(\lambda)$, where $F_0(\lambda)$ is the extraterrestrial solar irradiance (Thuillier et al., 2003). It is noted that $nL_w(\lambda)$ and $\rho_{wN}(\lambda)$ are interchangeable through a constant $\pi/F_0(\lambda)$. For empirical Chl-a algorithms, they can generally be written as:

$$\log_{10}[Chl\text{-}a] = \sum_{i=0}^{n} c_i r^i \quad (1)$$

where $r = max[\rho_{wN}(\lambda_1)/\rho_{wN}(\lambda_3), \rho_{wN}(\lambda_2)/\rho_{wN}(\lambda_3)]$, with *max* taking a larger value from two reflectance $\rho_{wN}(\lambda)$ ratios. Usually λ_1 and λ_2 are at blue bands, while λ_3 is at green wavelengths. The coefficients c_i's are those best fitting to the formulas. Specifically, the standard MODIS OC3M algorithm (O'Reilly et al., 1998, 2000) can be expressed as:

$$\log_{10}\left[Chl\text{-}a^{(OC3M)}\right] = 0.243 - 2.582r + 1.705r^2 - 0.341r^3 - 0.881r^4, \quad (2)$$

where $r = max[\rho_{wN}(443)/\rho_{wN}(551), \rho_{wN}(488)/\rho_{wN}(551)]$. The Arctic Ocean OC4L algorithm is written as (Cota et al., 2004):

$$\log_{10}\left[Chl\text{-}a^{(OC4L)}\right] = 0.592 - 3.607r, \quad (3)$$

where $r = max[\rho_{wN}(443)/\rho_{wN}(555), \rho_{wN}(490)/\rho_{wN}(555)]$. Finally the Bering Sea BS-OC algorithm (Naik et al., 2013) is:

$$\log_{10}\left[Chl\text{-}a^{(BS\text{-}OC)}\right] = 0.437 - 3.537r, \quad (4)$$

where $r = max[\rho_{wN}(443)/\rho_{wN}(555), \rho_{wN}(490)/\rho_{wN}(555)]$.

It should be noted that there is no 490 nm band for MODIS-Aqua, thus $\rho_{wN}(\lambda)$ at the band 488 nm was used for both $Chl\text{-}a^{(OC4L)}$ and $Chl\text{-}a^{(BS\text{-}OC)}$. The error introduced due to a slight difference in the wavelengths can be considered to be relatively small, compared to errors in the algorithm itself.

4. Evaluation and development of Chl-a algorithms

4.1. MODIS-Aqua-derived and in situ-measured $nL_w(\lambda)$ comparisons

MODIS-Aqua-derived $nL_w(\lambda)$ spectra were overestimated for all wavelengths compared to in situ measurements (Table 1), e.g., mean values of in situ $nL_w(\lambda)$ at wavelengths of 412, 443, 488, and 555 nm of 0.439, 0.566, 0.654, and 0.342 mW cm^{-2} μm^{-1} sr^{-1}, respectively, and the corresponding MODIS-Aqua-derived values of 0.509, 0.599, 0.668, and 0.393 mW cm^{-2} μm^{-1} sr^{-1}, respectively. In general, a good agreement was found between satellite and in situ matchups as shown for $nL_w(\lambda)$ at wavelengths of 412, 443, 488, and 555 nm for a time difference of 24 hours between satellite and in situ measurements (Fig. 2a and Table 1). However, the mean and median ratios of MODIS-Aqua to in situ $nL_w(\lambda)$ ranged from 1.097–1.280 and 1.052–1.242 (Fig. 2a and Table 1), respectively, with the best agreement being at 488 nm (Fig. 2a and Table 1).

Empirical ocean color algorithms for retrieval of Chl-a, as discussed previously (e.g., OCM3, Arctic-OC4L, BS-OC, etc.), all use blue-green $nL_w(\lambda)$ ratios (Cota et al., 2004; Naik et al., 2013; O'Reilly et al., 1998). To evaluate and understand the accuracy of Chl-a algorithms, it is essential to evaluate the performance of blue-green $nL_w(\lambda)$ ratios from satellite measurements. As long as these satellite-derived $nL_w(\lambda)$ ratios are satisfactorily compared to in situ matchup data, Chl-a algorithms can be developed or regionally tuned for better performance using these $nL_w(\lambda)$ ratio values. An analysis of the blue to green $nL_w(\lambda)$ ratios from MODIS-Aqua and in situ measurements for the study region show good correlation (Fig. 2b), i.e., the mean ratios in $nL_w(443)/nL_w(555)$ and $nL_w(488)/nL_w(555)$ were 1.009 and 0.942, respectively, thereby providing confidence in the development of regional Chl-a algorithms for the Bering Sea based on these $nL_w(\lambda)$ (or $\rho_{wN}(\lambda)$) ratios. Furthermore, results from the $nL_w(\lambda)$ ratio matchup analyses in Fig. 2b show that MODIS-Aqua-derived $nL_w(\lambda)$ ratios are quite accurate, and errors in satellite-derived Chl-a values in the Bering Sea are not primarily from the $nL_w(\lambda)$ ratio (i.e., atmospheric correction), but from the Chl-a algorithm itself (e.g., its applicability to the region).

Table 1
Statistics results of MODIS-derived and in situ-measured $nL_w(\lambda)$ in the eastern Bering Sea.

MODIS vs. in situ $nL_w(\lambda)$							
Wavelength (nm)	MODIS-Aqua		In situ		Analyses results		
	Mean[a]	Median[a]	Mean[a]	Median[a]	Mean ratio	RMSD[a]	Bias diff.[a]
412	0.509	0.439	0.439	0.358	1.280	0.136	0.082
443	0.599	0.528	0.566	0.489	1.190	0.109	0.052
488	0.668	0.633	0.654	0.598	1.097	0.081	0.030
555	0.393	0.419	0.342	0.345	1.164	0.071	0.054

[a] Unit in mW cm^{-2} μm^{-1} sr^{-1}.

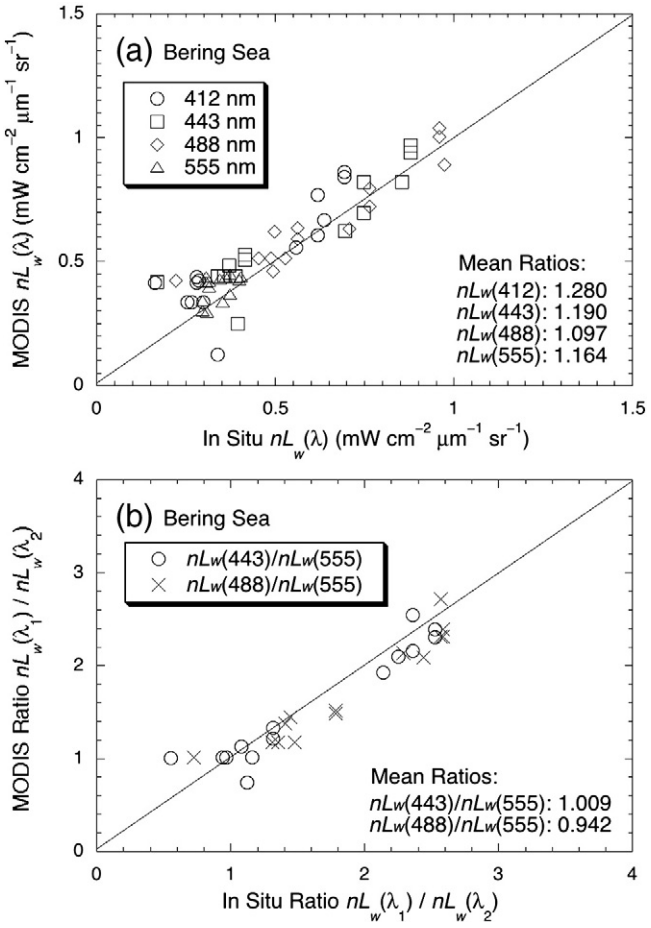

Fig. 2. Comparisons of (a) MODIS-Aqua-derived $nL_w(\lambda)$ with in situ-measured $nL_w(\lambda)$ at wavelengths of 412, 443, 488, and 555 nm, and (b) MODIS-Aqua-derived $nL_w(\lambda)$ ratio with in situ-measured $nL_w(\lambda)$ ratio between bands 443 and 555 nm, $nL_w(443)/nL_w(555)$, and 488 and 555 nm, $nL_w(488)/nL_w(555)$.

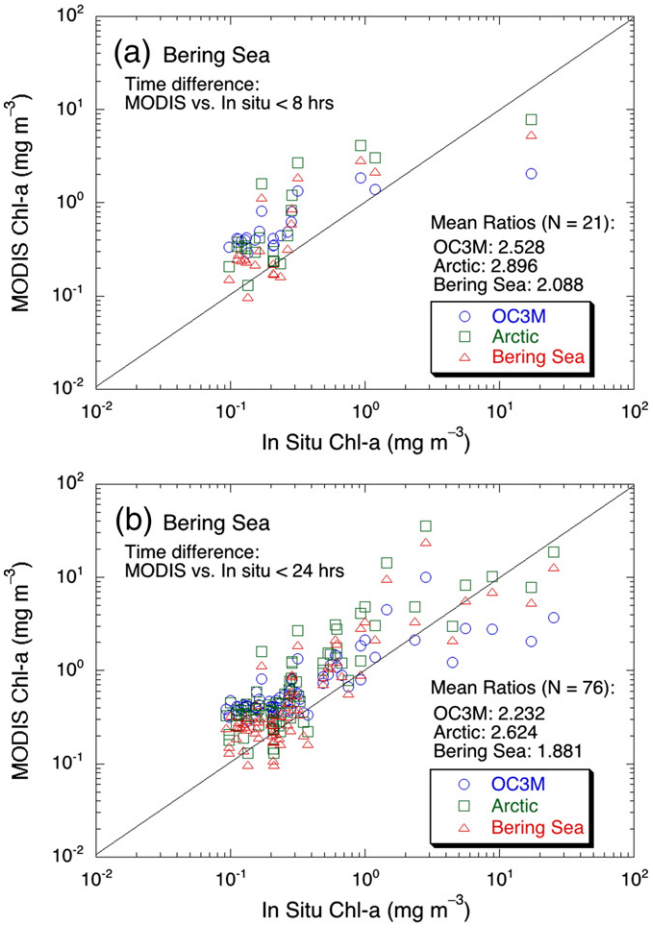

Fig. 3. Comparison of matchup results for time difference of (a) 8 h and (b) 24 h between MODIS-Aqua-derived and in situ-measured Chl-a data for cases of MODIS Chl-a data calculated using OC3M—the standard MODIS-Aqua Chl-a algorithm, OC4L—a Chl-a algorithm regionally tuned to the Arctic Ocean, and BS-OC—a Chl-a algorithm regionally tuned to the eastern Bering Sea.

4.2. MODIS-Aqua-derived and in situ-measured Chl-a comparisons

To evaluate the optimum time difference for obtaining a sufficient number of valid collocated satellite and in situ matchup data points, several temporal windows between satellite and in situ measurements have been examined. For the study region, Bailey and Werdell (2006) criteria were found to be too stringent to obtain adequate number of valid matchup points (only 13 matchup points for a 3 hour time difference). From our analysis, it was subjectively decided to use a 24-hour time difference as the optimal temporal window. This choice was based on the marked increase in the number of matchup points without any obvious impact on the statistics (Fig. 3 and Table 2). Although the number of valid matchup points was even larger for weekly averaged satellite data, it was decided not to use it for two reasons: the first was due to the high scatter that was observed between the matchups (standard deviation = 8.29), and second, it was believed that weekly data would average out too much of the environmental variability in the study region.

Three Chl-a algorithms have been examined for the study region, OC3M for the standard MODIS-Aqua algorithm for global open ocean (O'Reilly et al., 1998, 2000), Arctic-OC4L for an algorithm regionally tuned for the Arctic Ocean (Cota et al., 2004), and BS-OC for an algorithm regionally tuned to the Bering Sea (Naik et al., 2013). The results of these analyses are provided in Fig. 3 and Table 2. The mean ratios between MODIS and in situ Chl-a data within 8 hours for the OC3M, Arctic-OC4L, and BS-OC are 2.528, 2.896, and 2.088, respectively, compared with the corresponding values of 2.232, 2.624, and 1.881, respectively, for a time difference of 24 h. Table 2 provides statistics results (including mean ratio, root-mean-square deviation (RMSD), and bias difference) of MODIS-Aqua-derived versus in situ-measured data for the three Chl-a algorithms for cases with time differences of 8 and 24 hours, respectively. It is noted that RMSD values for Chl-a are calculated in log-scale (bias difference in linear scale). Chl-a comparison results are quite comparable for both time differences of 8 and 24 hours. Results in Fig. 3 show that the standard OC3M Chl-a algorithm

Table 2
Statistics of MODIS-derived and in situ-measured Chl-a in the eastern Bering Sea.

MODIS vs. in situ Chl-a			
Algorithm	Mean ratio	RMSD[a]	Bias Diff.[b]
Time difference ≤ 8 h			
OC3M	2.528	0.470	0.372
Arctic-OC4L	2.896	0.469	−0.133
BS-OC	2.088	0.372	0.208
Time difference ≤ 24 h			
OC3M	2.232	0.408	−0.239
Arctic-OC4L	2.624	0.428	0.886
BS-OC	1.881	0.332	0.260

[a] Calculated in log-scale.
[b] Unit in mg m^{-3}.

overestimates and underestimates Chl-a values at low and high concentrations, correspondingly, compared to the in situ data. Previous studies in the Bering Sea have shown that overestimation at low Chl-a values is due to the influence of CDOM, while underestimation at high Chl-a is attributed to package effect of phytoplankton pigments (Naik et al., 2013). Similar results were observed for the Arctic-OC4L and BS-OC, although the underestimation and overestimation were not as pronounced as those of OC3M. In fact, the BS-OC method showed the best performance among the three algorithms. However, the BS-OC algorithm tends to overestimate Chl-a data, compared to the in situ measurements (mean ratio = 1.881). As the existing empirical algorithms to retrieve Chl-a from MODIS-Aqua for the Bering Sea do not perform satisfactorily, a new blended Chl-a algorithm using MODIS-Aqua-derived $\rho_{wN}(\lambda)$ spectra has been developed and proposed.

4.3. A new blended Chl-a algorithm for the eastern Bering Sea

For the eastern Bering Sea, the current algorithms either underestimate or overestimate Chl-a values with the BS-OC showing better results among them. A previous Chl-a algorithm developed for the Bering Sea (i.e., BS-OC) was limited in its temporal range since the data used to develop the algorithm was collected during summer, and hence could not be expected to perform well for other seasons. Ideally, in order for satellite sensors to capture a broad range of Chl-a associated with strong seasonality of sea-ice in the Bering Sea, a suite of concurrent in situ measurements of $nL_w(\lambda)$ and Chl-a across the distinct seasons is required to develop Chl-a algorithms from in situ measurements that can then be applied to satellite data. To our knowledge, such concurrent measurements have not been obtained for the Bering Sea. However, a large dataset of Chl-a measurements were collected covering the distinct seasons as part of a multi-year National Science Foundation (NSF) funded study in the Bering Sea (i.e., BEST). Thus, a possible approach to deal with the lack of concurrent in situ measurements of $nL_w(\lambda)$ and Chl-a across the seasons is to use the in situ-measured Chl-a seasonally and the corresponding satellite-measured $nL_w(\lambda)$ data. In fact, most ocean color algorithms use reflectance $\rho_{wN}(\lambda)$ ratios, e.g., for Chl-a algorithm as discussed previously (O'Reilly et al., 1998). The relationships between blue or red and green $\rho_{wN}(\lambda)$ ratios from MODIS-Aqua versus in situ Chl-a data in the Bering Sea are shown in Fig. 4. A significant relationship with good correlation was observed between the satellite-derived $\rho_{wN}(\lambda)$ ratios and in situ Chl-a data, even though the MODIS-Aqua-derived $\rho_{wN}(\lambda)$ data differ spatially (1-km) and temporally (24 hours) from the in situ Chl-a measurements.

Similar results were observed using in situ-measured $\rho_{wN}(\lambda)$ and Chl-a obtained from the SeaBASS database for the Bering Sea. We could only make comparisons between the reflectance ratios in $\rho_{wN}(443)/\rho_{wN}(555)$ ($r(443,555)$) and $\rho_{wN}(488)/\rho_{wN}(555)$ ($r(488,555)$) since the SeaBASS data do not have any measurements for $\rho_{wN}(551)$. Remarkably, similar coefficients were observed from in situ data (i.e., $\log_{10}[\text{Chl-a}] = 0.723 - 2.144\cdot\log_{10}[r(443,555)]$) and satellite data (i.e., $\log_{10}[\text{Chl-a}] = 0.871 - 2.092\cdot\log_{10}[r(443,555)]$) between Chl-a versus reflectance ratio $r(443,555)$. The relatively small differences in the coefficients from satellite and in situ fittings can be attributed to several factors, such as the uncertainty from atmospheric correction that cause the satellite-derived $\rho_{wN}(\lambda)$ to differ from in situ $\rho_{wN}(\lambda)$ (e.g., Fig. 2), and the spatial (5×5 pixels averaging) and temporal (24 hours) variability.

Over the entire range of Chl-a, the ratio of $\rho_{wN}(443)/\rho_{wN}(551)$ (blue-green) shows the strongest correlation (Fig. 4a). However, on a closer examination we found that the blue and green $\rho_{wN}(\lambda)$ ratios perform better at a lower Chl-a concentration (<~1 mg m^{-3}), while the red-green $\rho_{wN}(\lambda)$ ratio perform better at a higher Chl-a concentration (>~1 mg m^{-3}) (Fig. 4c). In particular, the reflectance ratios in $\rho_{wN}(443)/\rho_{wN}(551)$ and $\rho_{wN}(488)/\rho_{wN}(551)$ are strongly correlated to Chl-a < ~1 mg m^{-3} with correlation coefficients of 0.910 and 0.834, respectively, whereas the ratio in $\rho_{wN}(667)/\rho_{wN}(551)$ has a good correlation to Chl-a for its values > ~1 mg m^{-3} with correlation coefficient of 0.881. It is particularly noted that the reflectance ratio in $\rho_{wN}(667)/\rho_{wN}(551)$ is quite sensitive to large Chl-a values >~1 mg m^{-3}. Hence, an algorithm that blends these two $\rho_{wN}(\lambda)$ ratios has been developed.

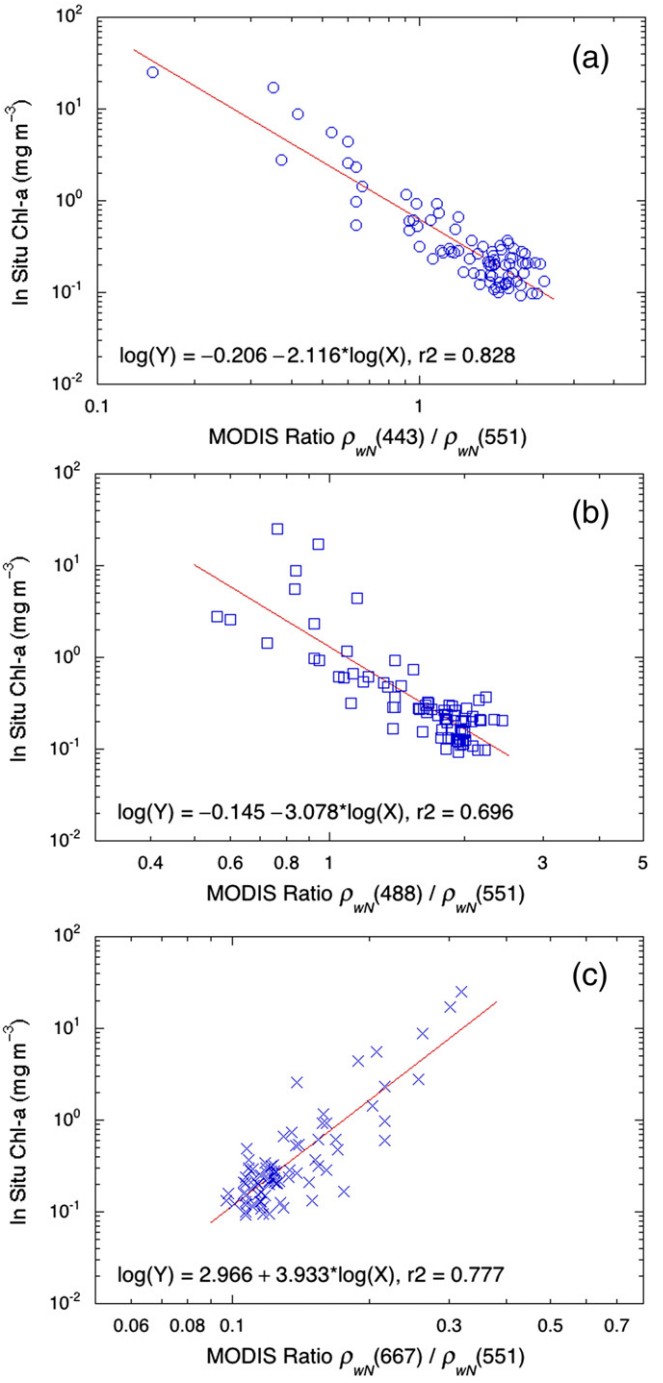

Fig. 4. In situ-measured Chl-a as a function of MODIS-Aqua-derived $\rho_{wN}(\lambda)$ ratio between bands (a) 443 and 551 nm, $\rho_{wN}(443)/\rho_{wN}(551)$, (b) 488 and 551 nm, $\rho_{wN}(488)/\rho_{wN}(551)$, and (c) 667 and 551 nm, $\rho_{wN}(667)/\rho_{wN}(551)$.

For low Chl-a concentrations, an algorithm that utilizes the maximum blue–green $\rho_{wN}(\lambda)$ ratio $r^{(B\text{-}G)}$ is proposed, i.e.,

$$\log_{10}\left[Chl\text{-}a^{(1)}\right] = -0.034 - 2.362\, r^{(B\text{-}G)}, \quad \text{for } r^{(B\text{-}G)} > 1.4, \tag{5}$$

where $r^{(B\text{-}G)} = max\,[\rho_{wN}(443)/\rho_{wN}(551), \rho_{wN}(488)/\rho_{wN}(551)]$, with *max* taking the larger value from two reflectance $\rho_{wN}(\lambda)$ ratios. On the

other hand, an algorithm that uses the red-green $\rho_{wN}(\lambda)$ ratio $r^{(R\text{-}G)}$ is developed, i.e.,

$$\log_{10}\left[Chl\text{-}a^{(2)}\right] = 3.140 + 4.160\, r^{(R\text{-}G)},\ \text{for}\ r^{(B\text{-}G)}<1.0, \tag{6}$$

where $r^{(R\text{-}G)} = \rho_{wN}(667)/\rho_{wN}(551)$. In producing regional Chl-a images, a realistic smooth transition between the two Chl-a algorithms is needed to avoid discontinuity between the distinct domains of the Bering Sea. Low blue-green $\rho_{wN}(\lambda)$ ratios were observed along the coast in the inner domain and high $\rho_{wN}(\lambda)$ ratios were observed off the continental slope in the deep Bering Sea basin with intermediate values elsewhere in the study region. To allow a smooth transition between the high and low $\rho_{wN}(\lambda)$ ratios, a weighting function that blends the two Chl-a models is defined, i.e.,

$$W = -2.5 + 2.0\, r^{(B\text{-}G)},\quad \text{for}\ 1.0 \le r^{(B\text{-}G)} \le 1.4. \tag{7}$$

Thus, the blended Chl-a model can be expressed as:

$$Chl\text{-}a = W\, Chl\text{-}a^{(1)} + (1-W)\, Chl\text{-}a^{(2)}, \tag{8}$$

where $Chl\text{-}a^{(1)}$ and $Chl\text{-}a^{(2)}$ are from Eqs. (5) and (6), respectively, and weight $W = 1$ for $W \ge 1$ and $W = 0$ for $W \le 0$, which are calculated according to Eq. (7).

In summary, for $r^{(B\text{-}G)} < 1.0$, Chl-a is calculated using Eq. (6), while for cases with $r^{(B\text{-}G)} > 1.4$ Chl-a is computed using Eq. (5). For all other $r^{(B\text{-}G)}$ values, i.e., $1.0 \le r^{(B\text{-}G)} \le 1.4$, Chl-a data are computed using Eq. (8) based on the weighting function calculated in Eq. (7). Evaluation of results shows that the blended scheme described above works well and produces Chl-a images without obvious discontinuities.

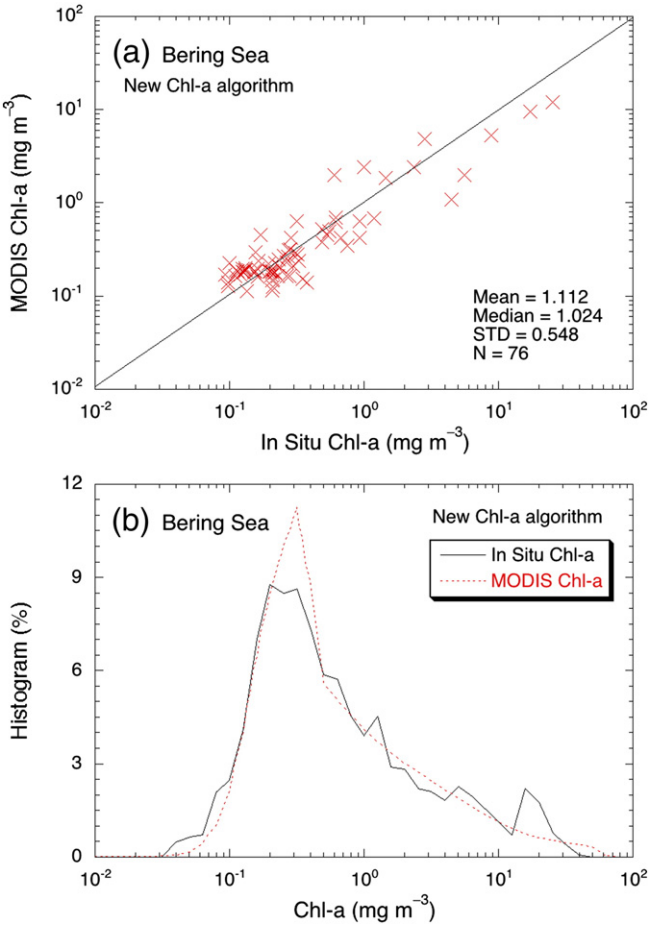

Fig. 5. MODIS-Aqua-derived Chl-a using the new blended Chl-a algorithm compared with the in situ data for (a) matchup comparison with scatter plot of MODIS versus in situ data and (b) histogram comparison results.

Fig. 5 shows the significantly improved Chl-a data from the blended Chl-a algorithm as demonstrated in the statistics results, such as mean and median ratios and STD values (Fig. 5a), in MODIS-Aqua-derived versus in situ-measured Chl-a data. The mean and median ratios between MODIS and in situ Chl-a data are 1.112 and 1.024 with STD of 0.548. In addition, in Fig. 5a the log-scale RMSD value is 0.212 (corresponding to Chl-a of 1.629 mg m^{-3}) and bias difference is −0.364 mg m^{-3}. The improved performance of the blended Chl-a algorithm for the Bering Sea is further validated by a good agreement of frequency distribution between the MODIS-Aqua-derived Chl-a using the blended algorithm and the in situ-measured Chl-a data in the Bering Sea (Fig. 5b). Both of the distributions peak at ~0.25 mg m^{-3}. The better performance of the newly developed blended Chl-a algorithm allows the assessment of long-term trends in phytoplankton biomass associated with climatic fluctuations in the Bering Sea.

5. MODIS-Aqua-derived $nL_w(\lambda)$ and Chl-a in the Bering Sea

5.1. Climatology of MODIS-Aqua-derived $nL_w(\lambda)$

Seasonal climatology images of MODIS-Aqua-derived $nL_w(\lambda)$ at 443, 488, 551, and 667 nm from July 2002 to December 2013 are shown in Fig. 6. Strong seasonal and spatial variability is observed in the study area (Figs. 6 and 7). The spatial distribution patterns of $nL_w(\lambda)$ are similar, showing highs near the coast and lows in the outer domain irrespective of wavelength. However, high $nL_w(\lambda)$ values near the coastal region are more apparent at wavelengths of 551 and 667 nm (green and red) compared to $nL_w(\lambda)$ at blue wavelengths (412 and 443 nm). The spatial patterns are not uniform even within each domain; localized spatial patterns are evident from the seasonal images. For example, in winter very high $nL_w(\lambda)$ values are shown at the center of the middle domain and low $nL_w(\lambda)$ values elsewhere. During spring and fall seasons, high $nL_w(\lambda)$ values are constrained within the central part of the inner and middle domains. On the eastern Bering Sea shelf, the seasonal peak in $nL_w(\lambda)$ values appears during winter, while the lowest values are observed during summer.

The seasonal mean $nL_w(\lambda)$ values were calculated from the seasonal climatology images for the inner, middle, and outer domains, as well as the basin region in the Bering Sea (Fig. 7). A strong wavelength dependent seasonal pattern in $nL_w(\lambda)$ is observed across all the regions, with the seasonal variability being more significant for $nL_w(\lambda)$ at the green and red bands relative to the blue bands. The seasonal patterns of $nL_w(\lambda)$ are similar in the inner and middle domains and different in the outer domain to a certain extent. In particular, the inner and middle domains show significantly high $nL_w(\lambda)$ values at the green and red wavelengths in winter, indicating more turbid waters in these regions. In contrast, the seasonal variability is much less pronounced in the outer domain relative to the other regions. The shelf (Fig. 7a–c) and basin (Fig. 7d) show contrasting seasonal patterns. While the highest $nL_w(\lambda)$ values are observed in winter and the lowest in summer for most wavelengths on the eastern shelf, the opposite $nL_w(\lambda)$ pattern is observed for the basin region at all wavelengths.

5.2. Climatology of MODIS-Aqua-derived Chl-a using the new blended algorithm

Seasonal climatology images of Chl-a derived using the newly developed blended Chl-a algorithm from MODIS-Aqua for the eastern Bering Sea are shown in Fig. 8. The eastern Bering Sea shelf region is characterized by high Chl-a concentrations throughout the year relative to the Bering Sea basin with marked seasonality (Lomas et al., 2012; Moran et al., 2012). High values of Chl-a near the coast are observed all year round, with wider coverage in spring and fall seasons. The spring bloom is evident in all the domains, while the fall bloom appears

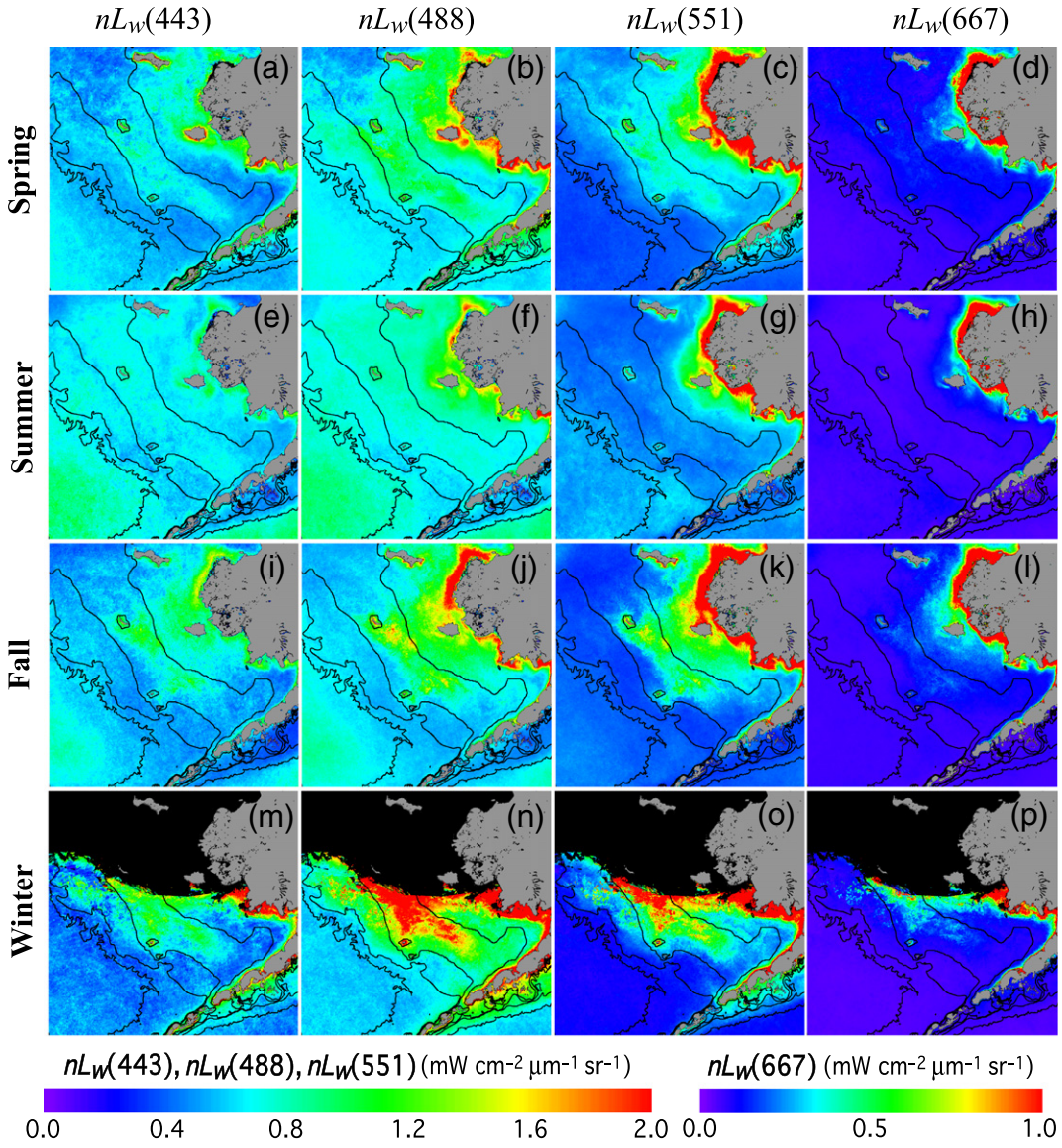

Fig. 6. Seasonal climatology images of MODIS-Aqua-derived $nL_w(\lambda)$ at 443, 488, 551, and 667 nm for (a–d) spring, (e–h) summer, (i–l) fall, and (m–p) winter. Color scale for $nL_w(443)$, $nL_w(488)$, and $nL_w(551)$ is 0–2 mW cm^{-2} µm^{-1} sr^{-1}, and for $nL_w(667)$ is 0–1 mW cm^{-2} µm^{-1} sr^{-1}.

clearly in the inner and middle domains. During summer, the shelf break region, the so-called 'green belt,' which is the most productive region of the Bering Sea, has relatively high values in contrast to low values in other regions. Indeed, Fig. 8 shows that the Chl-a seasonal variability in the eastern Bering Sea can be simply characterized by a spring bloom (April–May), a summer decrease (June–August), and a fall bloom (September–October). Previous studies (D'Sa, Miller, & McKee, 2007; Son & Wang, 2012; Tzortziou et al., 2007) have shown that, because reflectance $\rho_{wN}(\lambda)$ at the red band (or the reflectance ratio of red to green) is sensitive to backscattering, there will be a response to non-algal particles (sediments) in addition to phytoplankton. Thus, the elevated Chl-a values near the coast and during winter (intense mixing) may be an artifact of higher backscattering detected by the new blended algorithm. To address this limitation of the new blended algorithm, we have excluded Chl-a values greater than 40 mg m^{-3} in calculations of monthly and annual estimates shown in Figs. 9 and 10. Further, we found that using mean or median (or median with Chl-a $\leq$ 40 mg m^{-3}) in the monthly and annual estimates did not have a significant effect on trends shown in Figs. 9 and 10.

The monthly MODIS-Aqua-derived Chl-a values (median) from the blended Chl-a algorithm are shown in Fig. 9, demonstrating the distinct seasonality in Chl-a for the region. In all of the domains, there is a rapid Chl-a increase in spring from the low values in winter followed by a summer decrease, and then an increase again in fall. However, the timing of the spring bloom in each of the domains is different across the shelf. In general, the spring bloom begins in March steadily progressing across the shelf, starting in the inner domain followed by the middle and outer domain, and finally the shelf break over a course of ~2 months (Fig. 9). The fall bloom is clearly present in the inner and middle domains, and relatively less evident in the outer domain. In the basin region, however, Chl-a concentrations are quite low throughout the year with slightly elevated values in May–June.

5.3. Long-term trends of Chl-a in relation to the physical environment

The 11-years of MODIS-Aqua-derived Chl-a using the blended Chl-a algorithm shows the role of sea ice, SST, and wind speed in regulating the monthly and annual Chl-a trends in the eastern Bering Sea (Fig. 10). Overlaid on the annual cycle of Chl-a is the strong interannual variability closely linked to sea-ice concentration (Fig. 10b). Indeed, the complex interplay of these three major physical variables determines

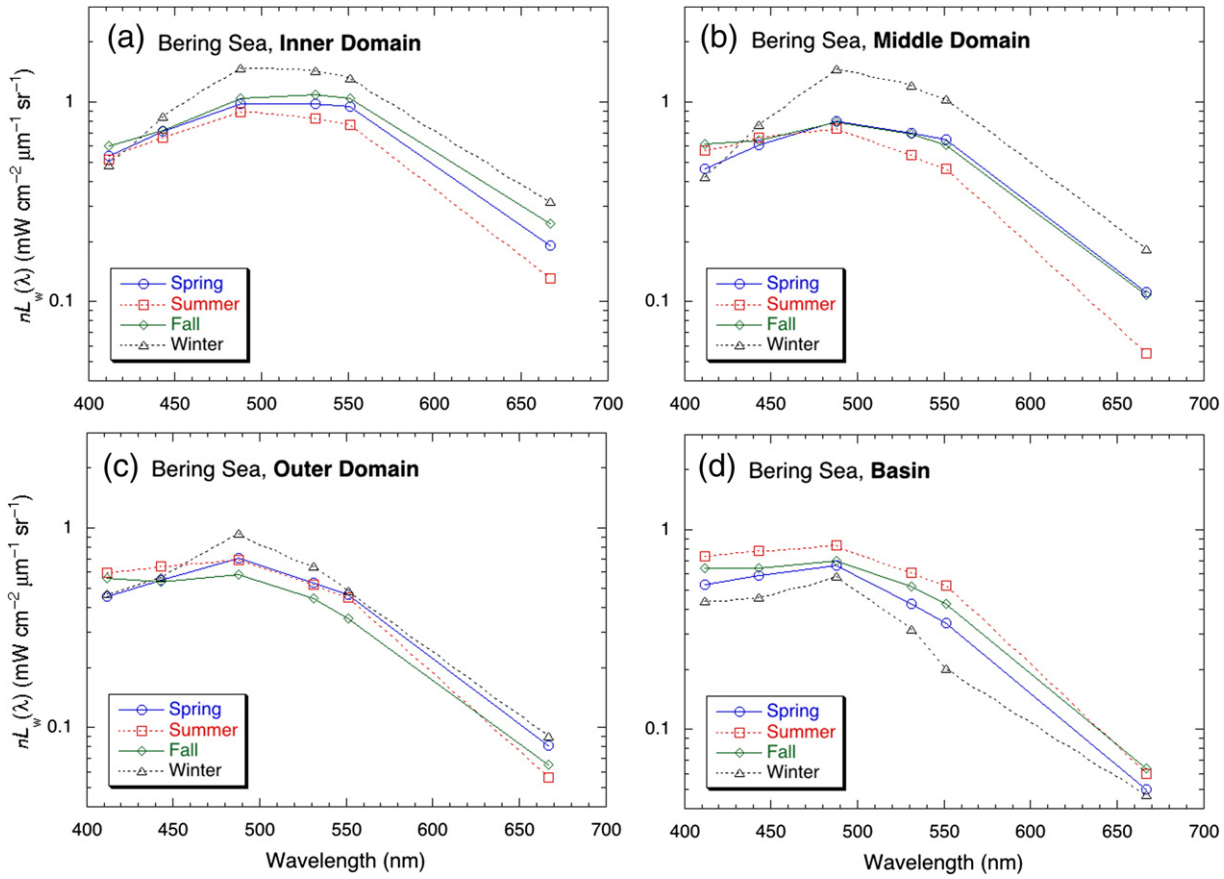

Fig. 7. Spectral characteristics of MODIS-Aqua-derived $nL_w(\lambda)$ for the region of (a) inner domain, (b) middle domain, (c) outer domain, and (d) basin region of the Bering Sea for spring, summer, fall, and winter seasons.

the timing and the fate of the spring phytoplankton bloom (Hunt et al., 2002; Sigler et al., 2014).

The sea ice extent, SST, and wind speed displayed strong seasonal patterns (Fig. 10a). SST is the lowest in winter and highest in summer (as expected), while wind speed is the weakest in summer and strongest in winter (Fig. 10a). The spring bloom is strongly associated with the sea ice retreat; more precisely, the timing of sea ice retreat determines whether there will be an ice edge bloom or open water bloom. Sea ice and SST in the Bering Sea are characterized by strong interannual variability. Chl-a peaks between March and April as the sea ice begins to recede, and then again to a lesser magnitude in October when storm induced mixing brings nutrients deeper in the water column to the surface. During the study period, the annual sea ice extent in the Bering Sea varied ~20% around its mean value of ~430,000 km^2. The years with the three lowest sea ice extent were 2003–2005, while the years of the three highest sea ice extent were 2009, 2010, and 2012 (Fig. 10b). The year 2012 was remarkable in sea ice coverage, reaching a record extent. Moreover, sea ice coverage in that year (and 2009) retreated the latest since 1985 (http://access.afsc.noaa.gov/reem/ecoweb/eco2012reportcardEBS.pdf). The sea ice coverage retreats within a period of ~1 month between May and June, while the sea ice coverage advances between September and October, or sometimes as late as November. A strong significantly negative correlation is found between annual mean sea ice extent and annual mean SST ($r^2 = 0.755$, $p = 0.001$). A significant increase in annual mean sea ice extent ($r^2 = 0.611$; $p = 0.008$) and decrease in annual mean SST ($r^2 = 0.844$; $p = 0.001$) are observed for the study period in the Bering Sea, with intense interannual variability, while the wind speed does not exhibit any significant trend ($p > 0.5$) (Fig. 10b).

It is hypothesized that during the warm years reduced sea ice coverage portends a longer growing season and high temperatures favor high phytoplankton growth, hence high Chl-a concentrations. In contrast, during the cold years, extensive sea ice coverage and low temperatures favor low phytoplankton growth rates, hence low Chl-a values (Lomas et al., 2012). Consistent with previous studies, in recent years the Bering Sea can be categorized into 'cold' and 'warm' years (Stabeno et al., 2012b). The years 2003–2005 can be categorized as 'warm' years, while the years 2007–2010 and 2012 can be categorized as 'cold' years for the study period. However, the corresponding Chl-a values grouped together between the 'warm' and 'cold' years are not significantly different, neither do they exhibit any significant changes over the entire study period ($p > 0.5$). Although the seasonal Chl-a changes appear coherent with sea ice and SST, interannual changes in Chl-a are more difficult to interpret. In fact, Chl-a exhibits no correlation to SST and sea ice extent over the entire study period. However, when the years with extreme sea ice extent and relatively high Chl-a (i.e., 2010 and 2012) are excluded, Chl-a in the region exhibits some meaningful negative and positive correlations with sea ice extent ($r = -0.78$; $p = 0.025$) and SST ($r = 0.75$; $p = 0.021$), respectively. For the entire period (including 2010 and 2012), correlation results for Chl-a and sea ice extent are ($r = 0.16$; $p = 0.66$), and results for Chl-a and SST are ($r = -0.19$; $p = 0.59$). The years 2009, 2010, and 2012 were very cold years, but Chl-a values displayed a varying range (Fig. 10b). Thus, even though we observed higher Chl-a values during warm years, equal or sometime higher annual mean Chl-a values were also shown in some cold years.

The magnitude of annual phytoplankton biomass is not as critical as timing of the spring phytoplankton bloom, which determines whether the benthic or the pelagic environment receives most of the primary

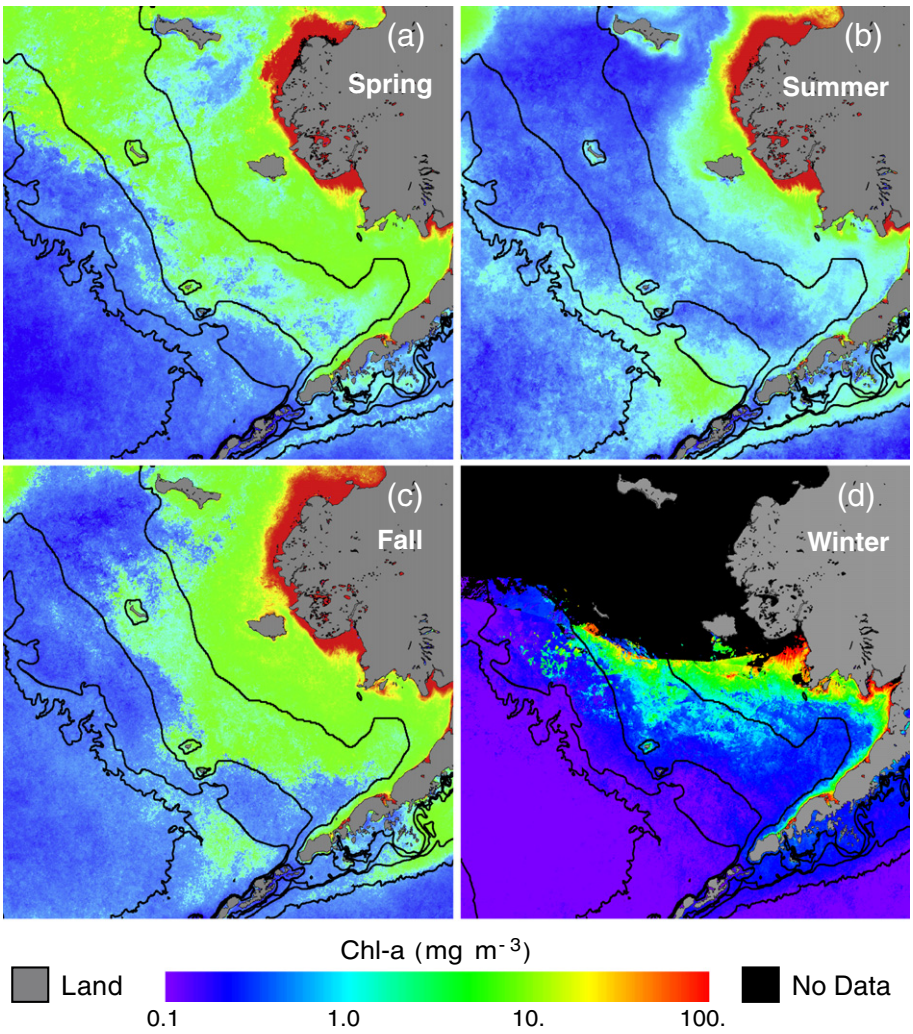

Fig. 8. MODIS-Aqua-derived seasonal Chl-a climatology images using the new blended Chl-a algorithm for (a) spring, (b) summer, (c) fall, and (d) winter.

production. During the cold years the spring bloom occurs early (March–April) and in cold waters (~1–2 °C), which is not efficiently grazed by zooplankton supporting a strong benthic habitat. Contrastingly, during the warm years the spring bloom occurs in relatively warm waters (~4–7 °C), with efficient grazing by zooplankton and most of the primary production is restricted to the pelagic environment (Hunt et al., 2002; Stabeno et al., 2012b). These results suggest that a complex interplay of the physical environment controls on the phytoplankton biomass, the extent of this control warrants further research and is beyond the scope of this paper.

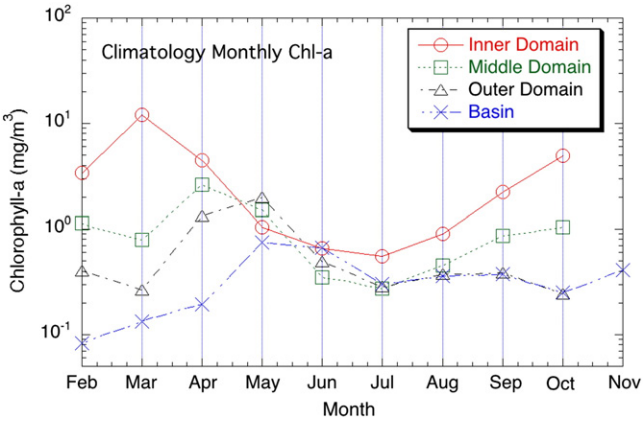

Fig. 9. MODIS-Aqua-derived monthly climatology Chl-a values using the new blended Chl-a algorithm for the inner domain, middle domain, outer domain, and the basin region in the Bering Sea.

6. Discussions and summary

Development of robust ocean color Chl-a algorithms for high-latitude oceanic regions from satellites is a challenge due to their unique bio-optical properties (Mitchell & Holm-Hansen, 1991; Sosik, Vernet, & Mitchell, 1992; Stramska, Stramski, Kaczmarek, Allison, & Schwarz, 2006; Wang, Cota, & Ruble, 2005). High-latitude oceanic regions are characterized by strong seasonality coupled with its variations in phytoplankton concentration and type (Lomas et al., 2012; Moran et al., 2012; Stramska et al., 2006). The seasonal changes in phytoplankton cause the species specific phytoplankton absorption to vary dramatically, with high values for smaller cells and low values for larger cells, which causes large differences in Chl-a retrievals from standard empirical algorithms (Mitchell & Holm-Hansen, 1991; Naik et al., 2013). Furthermore, high CDOM concentration contributes significantly to total light absorption at shorter wavelengths around the blue region, which causes Chl-a to be overestimated by standard Chl-a algorithms (Naik et al., 2013).

The work presented here incorporates a large seasonally and spatially wide in situ dataset to develop a robust Chl-a algorithm for the eastern Bering Sea. The first step towards this task was to validate the MODIS-Aqua $nL_w(\lambda)$ spectra as well as $nL_w(\lambda)$ ratios, which were

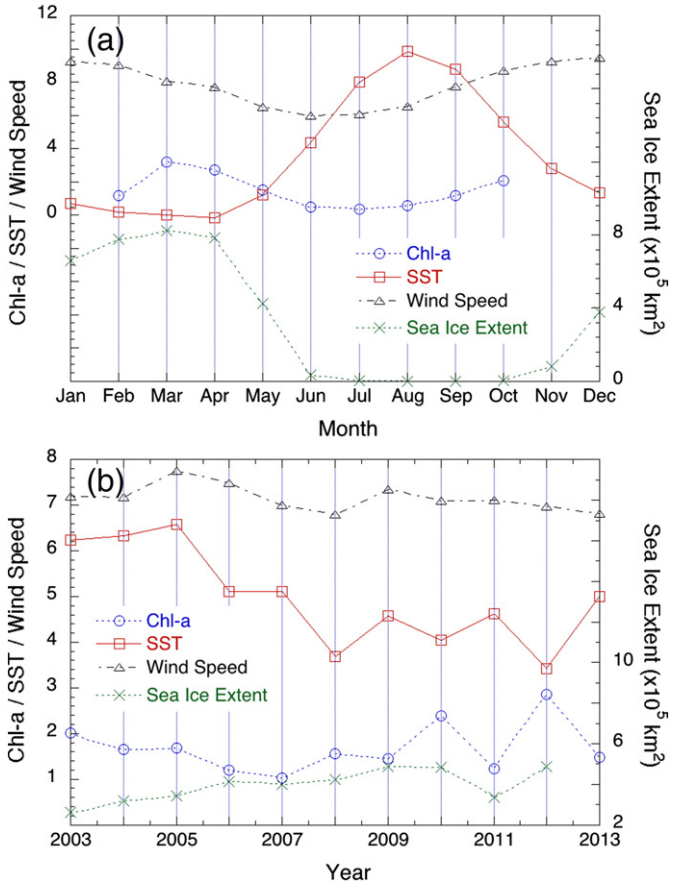

Fig. 10. (a) Monthly climatology and (b) annual time series of sea ice extent, SST, wind speed, and MODIS-Aqua-derived Chl-a using the new blended Chl-a algorithm for the eastern Bering Sea shelf. Units for Chl-a, SST, and wind speed are mg m^{-3}, °C, and m s^{-1}, respectively, and scaled in left, while the sea ice extent is in km^2 and scaled in the right.

derived using the NIR-SWIR combined atmospheric correction algorithm (Wang, 2007; Wang & Shi, 2007; Wang et al., 2009) with the NOAA-MSL12 ocean color data processing system. The MODIS-Aqua-derived $nL_w(\lambda)$ at individual wavelengths as well their ratios that go as inputs into the empirical Chl-a algorithms show good agreement with those from in situ measurements. In fact, the performance of atmospheric correction in the Bering Sea using the NOAA-MSL12 is consistent with those from various other regions, e.g., the Chesapeake Bay region (Son & Wang, 2012), the China east coastal region (Wang, Tang, & Shi, 2007), China's inland Lake Taihu (Wang, Shi, & Tang, 2011), and global ocean data (Wang et al., 2009), as well as measurements from other satellite sensors (Wang, Shi, & Jiang, 2012, 2013a, 2013b; Wang et al., 2013a, 2013b).

Although several empirical and semi-analytical algorithms have been developed to compute Chl-a, only few of them have been specifically developed for high latitude waters. We examined three Chl-a algorithms to verify their performance for the eastern Bering Sea, namely the standard MODIS-Aqua Chl-a algorithm OC3M, an algorithm tuned for the Arctic, OC4L, and an algorithm tuned for the Bering Sea, BS-OC. Out of the three the BS-OC performed the best, however, it still overestimated Chl-a in the region. The new Chl-a algorithm proposed here reduced these errors by using a blended approach, in particular, using water-leaving reflectance signal from the red band. This idea is similar to some other approaches using $nL_w(\lambda)$ at the red and NIR wavelengths for coastal waters (Gitelson, Schalles, & Hladik, 2007). In the blended approach we used two MODIS-Aqua-derived band ratios to estimate Chl-a, i.e., at low Chl-a concentrations the blue to green ratio ($\rho_{wN}(443)/\rho_{wN}(551)$) or ($\rho_{wN}(488)/\rho_{wN}(551)$) is used, while for higher Chl-a concentration the red to green reflectance ratio ($\rho_{wN}(667)/\rho_{wN}(551)$) is used. Frequency distribution histograms showed that Chl-a data derived using the blended Chl-a algorithm are very similar to the in situ Chl-a measurements, since both of the histograms peak at ~0.25 mg m^{-3}. The blended Chl-a algorithm proposed here can be applied to other high latitude offshore regions. However, like any other empirical model the algorithm coefficients will likely have to be tuned to the region of interest.

The blended Chl-a algorithm has been applied to long-term MODIS-Aqua measurements from 2002–2013. In addition, we analyzed long-term MODIS-Aqua-derived $nL_w(\lambda)$ spectra data. To our knowledge it is the first time that validated $nL_w(\lambda)$ and Chl-a derived from a regionally tuned algorithm with relatively low uncertainties have been analyzed for the Bering Sea. We found that, although similar Chl-a trends (qualitatively) can be derived using the MODIS standard OC3M algorithm for the region, there are obvious differences (some are significant) in the magnitude of the peaks and troughs in the trends, which are also quite important.

The $nL_w(\lambda)$ composite images and time series show that there is strong seasonal variability in $nL_w(\lambda)$ for various regions in the Bering Sea. This seasonal variability is more pronounced for the green and red bands relative to the blue bands. On the eastern Bering Sea shelf, the seasonal highs and lows in $nL_w(\lambda)$ appear in winter and summer, respectively. Some of the localized high values observed during winter and late fall are probably due to mixing caused by storm events.

The long-term MODIS-Aqua-derived Chl-a data using the new Chl-a algorithm have been also studied in relations to sea ice, SST, and wind speed in the Bering Sea. The spatial and temporal patterns of Chl-a are consistent with those observed in primary productivity, with high spatial and annual variability (Lomas et al., 2012; Mueter et al., 2009). From the seasonal composite images, the distinct spatial patterns of spring and fall blooms are clearly evident; while the spring bloom extended to all the three domains and the entire shelf, the fall bloom is restricted to the inner and middle domains and southern shelf region. The spatial patterns of Chl-a are consistent with those seen in primary productivity (Lomas et al., 2012). In fact, the spring bloom progresses from the inner shelf towards the outer shelf in a period of ~2 months. A similar progression of the spring bloom in the region was seen from the in situ measured primary productivity data (Lomas et al., 2012; Rho & Whitledge, 2007).

The interannual variability is closely linked to variability in the physical environment. A complex interplay of sea ice, SST, and wind speed determine the timing, intensity, and the fate of the spring bloom (Hunt et al., 2002; Lomas et al., 2012; Stabeno et al., 2012a). For a given year, one of these variables or a combination of them influences the timing and type of spring bloom. During warm years, Chl-a is expected to be high owing to a longer growing season and higher phytoplankton growth rate. On the other hand, during cold years shorter growing season and lower phytoplankton growth rates would result in lower Chl-a (Lomas et al., 2012; Mueter et al., 2009). Brown, van Dijken, and Arrigo (2011) observed that years with low sea ice cover (e.g., 2003) were associated with high SSTs and Chl-a, while years with high ice cover (e.g., 1999) were associated with low SSTs and Chl-a. However, they also show that relatively low Chl-a was observed with relatively low ice coverage (e.g., 2007), and high Chl-a with relatively high ice coverage (e.g., 2006). Furthermore, Brown and Arrigo (2013) observed that years with early sea ice retreat exhibited elevated net primary production. After excluding 2010 and 2012 (extensive ice coverage), we observed some slight differences in Chl-a between warm (2003–2005) (mean Chl-a of 1.786 mg m^{-3}) and cold (2007–2009) years (mean Chl-a of 1.347 mg m^{-3}) (Fig. 10b), which are consistent with results from Brown et al. (2011). For the 11-year period of our study, Chl-a did show some correlations with sea ice and SST when cases with high Chl-a and extensive sea ice extent (2010 and 2012) are excluded. Also, after excluding 2010 and 2012, results in Fig. 10b show that there is no significant trending in Chl-a since 2007.

The Bering Sea responds to a range of physical driving forces, from regional episodic events to interannual and decadal scales (Schumacher & Alexander, 1999; Stabeno et al., 1999, 2001). The interannual and decadal variabilities are likely to remain high as observed from the period of warm years and cold years, hence making it difficult to predict changes in the Bering Sea ecosystem. A long-term monitoring of the eastern Bering Sea ecosystem is necessary to understand the impacts of such variability on its rich biota. The new blended Chl-a algorithm proposed in this study can be applied to MODIS-Aqua as well as ocean color data from other sensors (e.g., SeaWiFS, VIIRS, etc.) to obtain a more accurate long-term Chl-a record in order to advance our understanding on the likely impacts of climate change on the Bering Sea ecosystem.

Acknowledgments

Some in situ $nL_w(\lambda)$ and Chl-a data were from the NASA SeaBASS database. The authors are grateful to the all scientists and investigators who contributed these valuable in situ data. Funding for this project was partially provided by NASA grants NNX07AR15G and NNX10AP10G to E. D'Sa, J. Goes and C. Mouw, NSF grants 0732640, 0732430 and 1107250 to C. Mordy, and NSF grant 0813985 to R. Sonnerup. The authors are grateful to F. Menzia, P. Proctor and E. Wisegarver for analysis of in situ data. The BEST project was partially funded by the Joint Institute for the Study of the Atmosphere and Ocean (JISAO) under NOAA Cooperative Agreements NA17RJ1232 and NA10OAR4320148, and is contribution 2269 to NOAA's Ecosystems and Fisheries-Oceanography Coordinated Investigations, contribution 2255 to JISAO, contribution 4202 to NOAA's Pacific Marine Environmental Laboratory, and BEST—BSIERP publication number 142. The views, opinions, and findings contained in this paper are those of the authors and should not be construed as an official NOAA or U.S. Government position, policy, or decision.

References

Aiken, J., Moore, G. F., & Hotligan, P. M. (1992). Remote sensing of oceanic biology in relation to global climate change. *Journal of Phycology*, *28*, 579–590.

Bailey, S. W., & Werdell, P. J. (2006). A multi-sensor approach for the on-orbit validation of ocean color satellite data products. *Remote Sensing of Environment*, *102*, 12–23.

Behrenfeld, M. J., & Falkowski, P. G. (1997). Photosynthetic rates derived from satellite-based chlorophyll concentration. *Limnology and Oceanography*, *42*, 1–20.

Behrenfeld, M. J., O'Malley, R. T., Siegel, D. A., McClain, C. R., Sarmiento, J. L., Feldman, G. C., et al. (2006). Climate-driven trends in contemporary ocean productivity. *Nature*, *444*, 752–755.

Behrenfeld, M. J., Randerson, J. T., McClain, C. R., Feldman, G. C., Los, S. O., Tucker, C. J., et al. (2001). Biospheric primary production during an ENSO transition. *Science*, *291*, 2594–2597.

Brown, Z. W., & Arrigo, K. R. (2013). Sea ice impacts on spring bloom dynamics and net primary production in the Eastern Bering Sea. *Journal of Geophysical Research, Oceans*, *118*, 43–62. http://dx.doi.org/10.1029/2012JC008034.

Brown, Z. W., van Dijken, G. L., & Arrigo, K. R. (2011). A reassessment of primary production and environmental change in the Bering Sea. *Journal of Geophysical Research*, *116*, C08014. http://dx.doi.org/10.1029/2010JC006766.

Coachman, L. K. (1986). Circulation, water masses, and fluxes on the southeastern Bering Sea shelf. *Continental Shelf Research*, *5*, 23–108.

Cota, G. F., Wang, H., & Comiso, J. C. (2004). Transformation of global satellite chlorophyll retrievals with a regionally tuned algorithm. *Remote Sensing of Environment*, *90*, 373–377. http://dx.doi.org/10.1016/j.rse.2004.01.005.

Coyle, K. O., Eisner, L. B., Mueter, F. J., Pinchuk, A. I., Janout, M. A., Cieciel, K. D., et al. (2011). Climate change in the southeastern Bering Sea: impacts on pollock stocks and implications for the oscillating control hypothesis. *Fisheries Oceanography*, *20*(2), 139–156.

D'Sa, Eurico J., Miller, Richard L., & McKee, Brent A. (2007). Suspended particulate matter dynamics in coastal waters from ocean color: application to the northern Gulf of Mexico. *Geophysical Research Letters*, *34*(23). http://dx.doi.org/10.1029/2007GL031192.

Gitelson, A. A., Schalles, J. F., & Hladik, C. M. (2007). Remote chlorophyll-a retrieval in turbid, productive estuaries: Chesapeake Bay case study. *Remote Sensing of Environment*, *109*, 464–472. http://dx.doi.org/10.1016/j.rse.2007.01.016.

Gordon, H. R. (2005). Normalized water-leaving radiance: revisiting the influence of surface roughness. *Applied Optics*, *44*, 241–248.

Gordon, H. R., & Wang, M. (1994). Retrieval of water-leaving radiance and aerosol optical thickness over the oceans with SeaWiFS: a preliminary algorithm. *Applied Optics*, *33*, 443–452.

Grebmeier, J. M., & Cooper, L. W. (1995). Influence of the St. Lawrence Island polynya upon the Bering Sea benthos. *Journal of Geophysical Research: Oceans (1978–2012)*, *100*, 4439–4460.

Grebmeier, J. M., Overland, J. E., Moore, S. E., Farley, E. V., Carmack, E. C., Cooper, L. W., et al. (2006). A major ecosystem shift in the northern Bering Sea. *Science*, *311*, 1461–1464. http://dx.doi.org/10.1126/science.1121365.

Hunt, G. L., Jr., Coyle, K. O., Eisner, L., Farley, E., Heintz, R., Mueter, F., et al. (2011). Climate impacts on eastern Bering Sea food webs: a synthesis of new data and an assessment of the oscillating control hypothesis. *ICES Journal of Marine Science*, *68*(6), 1230–1243. http://dx.doi.org/10.1093/icesjms/fsr036 (2011).

Hunt, G. L., Jr., & Stabeno, P. J. (2002). Climate change and the control of energy flow in the southeastern Bering Sea. *Progress in Oceanography*, *55*, 5–22.

Hunt, G. L., Jr., Stabeno, P., Walters, G., Sinclair, E., Brodeur, R. D., Napp, J. M., et al. (2002). Climate change and control of the southeastern Bering Sea pelagic ecosystem. *Deep Sea Research Part II: Topical Studies in Oceanography*, *49*, 5821–5853.

IOCCG (2010). Atmospheric correction for remotely-sensed ocean-colour products. In M. Wang (Ed.), *Reports of International Ocean-Color Coordinating Group, No. 10*. Dartmouth, Canada: IOCCG.

Jiang, L., & Wang, M. (2013). Identification of pixels with stray light and cloud shadow contaminations in the satellite ocean color data processing. *Applied Optics*, *52*, 6757–6770.

Kachel, N. B., Hunt, G. L., Salo, S. A., Schumacher, J. D., Stabeno, P. J., & Whitledge, T. E. (2002). Characteristics and variability of the inner front of the southeastern Bering Sea. *Deep Sea Research Part II: Topical Studies In Oceanography*, *49*, 5889–5909.

Kotwicki, S., Buckley, T. W., Honkalehto, T., & Walters, G. (2005). Variation in the distribution of walleye pollock (*Theragra chalcogramma*) with temperature and implications for seasonal migration. *Fishery Bulletin*, *103*, 574–587.

Leblanc, K., Hare, C., Boyd, P., Bruland, K., Sohst, B., Pickmere, S., et al. (2005). Fe and Zn effects on the Si cycle and diatom community structure in two contrasting high and low-silicate HNLC areas. *Deep Sea Research Part I: Oceanographic Research Papers*, *52*, 1842–1864.

Lomas, M. W., Moran, S. B., Casey, J. R., Bell, D. W., Tiahlo, M., Whitefield, J., et al. (2012). Spatial and seasonal variability of primary production on the Eastern Bering Sea shelf. *Deep Sea Research Part II: Topical Studies in Oceanography*, *65–70*, 126–140. http://dx.doi.org/10.1016/j.dsr2.2012.02.010.

Mathis, J. T., Cross, J. N., Bates, N. R., Moran, S. B., Lomas, M. W., Mordy, C. W., et al. (2010). Seasonal distribution of dissolved inorganic carbon and net community production on the Bering Sea shelf. *Biogeosciences*, *7*, 1769–1787. http://dx.doi.org/10.5194/bg-7-1769-2010.

Matsuoka, A., Huot, Y., Shimada, K., Saitoh, S. I., & Babin, M. (2007). Bio-optical characteristics of the western Arctic Ocean: implications for ocean color algorithms. *Canadian Journal of Remote Sensing*, *33*, 503–518.

McRoy, C., Hansell, D., Springer, A., Walsh, J., & Whitledge, T. (1987). Global maximum of primary production in the north Bering Sea. *Eos, Transactions of the American Geophysical Union*, *68*, 17–27.

McRoy, P. C., Hood, D. W., Coachman, L., Walsh, J. J., & Goering, J. J. (1986). Processes and resources of the Bering Sea shelf (PROBES): the development and accomplishments of the project. *Continental Shelf Research*, *5*, 5–21.

Mitchell, B. G., & Holm-Hansen, O. (1991). Bio-optical properties of Antarctic Peninsula waters — differentiation from temperate ocean models. *Deep Sea Research Part I: Oceanographic Research Papers*, *38*, 1009–1028.

Moran, S. B., Lomas, M. W., Kelly, R. P., Gradinger, R., Iken, K., & Mathis, J. T. (2012). Seasonal succession of net primary productivity, particulate organic carbon export, and autotrophic community composition in the eastern Bering Sea. *Deep Sea Research Part II: Topical Studies in Oceanography*, *65–70*, 84–97. http://dx.doi.org/10.1016/j.dsr2.2012.02.011.

Morel, A., & Gentili, B. (1996). Diffuse reflectance of oceanic waters. III. Implication of bidirectionality for the remote-sensing problem. *Applied Optics*, *35*, 4850–4862.

Mueter, F. J., Broms, C., Drinkwater, K. F., Friedland, K. D., Hare, J. A., Hunt, G. L., Jr., et al. (2009). Ecosystem responses to recent oceanographic variability in high-latitude Northern Hemisphere ecosystems. *Progress in Oceanography*, *81*, 93–110.

Mueter, F. J., & Litzow, M. A. (2008). Sea ice retreat alters the biogeography of the Bering Sea continental shelf. *Ecological Applications*, *18*, 309–320.

Naik, P., D'Sa, E. J., Gomes, H. R., Goés, J. I., & Mouw, C. B. (2013). Light absorption properties of southeastern Bering Sea waters: analysis, parameterization and implications for remote sensing. *Remote Sensing of Environment*, *134*, 120–134.

Niebauer, H., Alexander, V., & Cooney, R. (1981). Primary production at the Eastern Bering Sea ice edge: the physical and biological regimes. *The Eastern Bering Sea Shelf: Oceanography and Resources*, *2*, 763–772.

Niebauer, H. J., Bond, N. A., Yakunin, L. P., & Plotnikov, V. V. (1999). An update on the climatology and sea ice of the Bering Sea. *Dynamics of the Bering Sea*, 29–59.

O'Reilly, J. E., Maritorena, S., Siegel, D. A., O'Brien, M. C., Toole, D., Mitchell, B. G., et al. (2000). Ocean color chlorophyll a algorithms for SeaWiFS, OC2, and OC4: Version 4. *SeaWiFS Postlaunch Calibration and Validation Analyses, Part*, *3*, 9–23.

O'Reilly, J. E., Maritorena, S., Mitchell, B. G., Siegel, D. A., Carder, K. L., Garver, S. A., et al. (1998). Ocean color chlorophyll algorithms for SeaWiFS. *Journal of Geophysical Research*, *103*, 24937–24953. http://dx.doi.org/10.1029/98jc02160.

Overland, J. E., & Stabeno, P. J. (2004). Is the climate of the Bering Sea warming and affecting the ecosystem? *Eos, Transactions American Geophysical Union*, *85*, 309–312.

Ramachandran, S., & Wang, M. (2011). Near-real-time ocean color data processing using ancillary data from the Global Forecast System model. *Geoscience and Remote Sensing, IEEE Transactions on*, *49*, 1485–1495.

Rho, T., & Whitledge, T. E. (2007). Characteristics of seasonal and spatial variations of primary production over the southeastern Bering Sea shelf. *Continental Shelf Research*, *27*, 2556–2569.

Salomonson, V. V., Barnes, W. L., Maymon, P. W., Montgomery, H. E., & Ostrow, H. (1989). MODIS: Advanced facility instrument for studies of the Earth as a system. *IEEE Transactions on Geoscience and Remote Sensing*, *27*, 145–153.

Sambrotto, R., Niebauer, H., Goering, J., & Iverson, R. (1986). Relationships among vertical mixing, nitrate uptake, and phytoplankton growth during the spring bloom in the southeast Bering Sea middle shelf. *Continental Shelf Research*, *5*, 161–198.

Schallenberg, C., Lewis, M. R., Kelley, D. E., & Cullen, J. J. (2008). Inferred influence of nutrient availability on the relationship between sun-induced chlorophyll fluorescence and incident irradiance in the Bering Sea. *Journal of Geophysical Research*, *113*, C07046. http://dx.doi.org/10.1029/2007jc004355.

Schumacher, J. D., & Alexander, V. (1999). Variability and influence of the physical environment to the ecosystem in the Bering Sea. In K. O. T. R. Loughlin (Ed.), *The Bering Sea: A Summary Of Physical, Chemical And Biological Characteristics And A Synopsis Of Research* (pp. 147–160). North Pacific Marine Science Organization, PISCES, Alaska Sea Grant Press.

Schumacher, J. D., & Stabeno, P. J. (1998). *The Continental Shelf Of The Bering Sea.* New York, NY: John Wiley and Sons, Inc.

Shi, W., & Wang, M. (2007). Detection of turbid waters and absorbing aerosols for the MODIS ocean color data processing. *Remote Sensing of Environment*, *110*, 149–161.

Sigler, M. F., Harvey, H. R., Ashjian, C. J., Lomas, M. W., Napp, J. M., Stabeno, P. J., et al. (2010). How does climate change affect the Bering Sea ecosystem? *EOS, Transactions*, *91*, 457.

Sigler, M. F., Stabeno, P. J., Eisner, L. B., Napp, J. M., & Mueter, F. J. (2014). Spring and fall phytoplankton blooms in a productive subarctic ecosystem, the eastern Bering Sea, during 1995–2011. *Deep Sea Research Part II: Topical Studies in Oceanography*, *109*, 71–83.

Son, S., & Wang, M. (2012). Water properties in Chesapeake Bay from MODIS-Aqua measurements. *Remote Sensing of Environment*, *123*, 163–174.

Son, S., Wang, M., & Harding, L. W., Jr. (2014). Satellite-measured net primary production in the Chesapeake Bay. *Remote Sensing of Environment*, *144*, 109–119.

Sosik, H. M., Vernet, M., & Mitchell, A. D. (1992). A comparison of particulate absorption properties between high- and mid-latitude surface waters. *Antarctic Journal of the United States*, *27*, 162–164.

Springer, A. M., & McRoy, C. P. (1993). The paradox of pelagic food webs in the northern Bering Sea—III. Patterns of primary production. *Continental Shelf Research*, *13*, 575–599.

Springer, A. M., McRoy, C. P., & Flint, M. V. (1996). The Bering Sea Green Belt: shelf-edge processes and ecosystem production. *Fisheries Oceanography*, *5*, 205–223.

Stabeno, P., Bond, N., Kachel, N., Salo, S., & Schumacher, J. (2001). On the temporal variability of the physical environment over the south-eastern Bering Sea. *Fisheries Oceanography*, *10*, 81–98.

Stabeno, P. J., Farley, E. V., Jr., Kachel, N. B., Moore, S., Mordy, C. W., Napp, J. M., et al. (2012a). A comparison of the physics of the northern and southern shelves of the eastern Bering Sea and some implications for the ecosystem. *Deep Sea Research Part II: Topical Studies in Oceanography*, *65–70*, 14–30. http://dx.doi.org/10.1016/j.dsr2.2012.02.019.

Stabeno, P. J., Hunt, G. L., Jr., Napp, J. M., & Schumacher, J. D. (2006). *Physical Forcing Of Ecosystem Dynamics On The Bering Sea Shelf.* Cambridge, MA: Harvard University Press.

Stabeno, P. J., Kachel, N. B., Moore, S. E., Napp, J. M., Sigler, M., Yamaguchi, A., et al. (2012b). Comparison of warm and cold years on the southeastern Bering Sea shelf and some implications for the ecosystem. *Deep Sea Research Part II: Topical Studies in Oceanography*, *65–70*, 31–45. http://dx.doi.org/10.1016/j.dsr2.2012.02.020.

Stabeno, P. J., Schumacher, J. D., & Ohtani, K. (1999). The physical oceanography of the Bering Sea. *Dynamics of the Bering Sea*, 1–28.

Stramska, M., Stramski, D., Kaczmarek, S., Allison, D. B., & Schwarz, J. (2006). Seasonal and regional differentiation of bio-optical properties within the north polar Atlantic. *Journal of Geophysical Research*, *111*, C08003. http://dx.doi.org/10.1029/2005jc003293.

Thuillier, G., Herse, M., Labs, D., Foujols, T., Peetermans, W., Gillotay, D., et al. (2003). The solar spectral irradiance from 200 to 2400 nm as measured by the SOLSPEC spectrometer from the ATLAS and EURECA missions. *Solar Physics*, *214*, 1–22.

Tzortziou, M., Subramaniam, A., Herman, J. R., Gallegos, C. L., Neale, P. J., & Harding, L. W., Jr. (2007). Remote sensing reflectance and inherent optical properties in the mid Chesapeake Bay. *Estuarine, Coastal and Shelf Science*, *72*(1), 16–32.

Walsh, J. J., & McRoy, C. P. (1986). Ecosystem analysis in the southeastern Bering Sea. *Continental Shelf Research*, *5*, 259–288.

Wang, M. (1999). A sensitivity study of the SeaWiFS atmospheric correction algorithm: effects of spectral band variations. *Remote Sensing of Environment*, *67*, 348–359.

Wang, M. (2005). A refinement for the Rayleigh radiance computation with variation of the atmospheric pressure. *International Journal of Remote Sensing*, *26*, 5651–5663.

Wang, M. (2006a). Effects of ocean surface reflectance variation with solar elevation on normalized water-leaving radiance. *Applied Optics*, *45*, 4122–4128.

Wang, M. (2006b). Aerosol polarization effects on atmospheric correction and aerosol retrievals in ocean color remote sensing. *Applied Optics*, *45*, 8951–8963.

Wang, M. (2007). Remote sensing of the ocean contributions from ultraviolet to near-infrared using the shortwave infrared bands: simulations. *Applied Optics*, *46*, 1535–1547.

Wang, M., Ahn, J. -H., Jiang, L., Shi, W., Son, S., Park, Y. -J., et al. (2013a). Ocean color products from the Korean Geostationary Ocean Color Imager (GOCI). *Optics Express*, *21*, 3835–3849.

Wang, J., Cota, G. F., & Ruble, D. A. (2005). Absorption and backscattering in the Beaufort and Chukchi Seas. *Journal of Geophysical Research*, *110*, C04014. http://dx.doi.org/10.1029/2002jc001653.

Wang, M., & Franz, B. A. (2000). Comparing the ocean color measurements between MOS and SeaWiFS: a vicarious intercalibration approach for MOS. *Geoscience and Remote Sensing, IEEE Transactions on*, *38*, 184–197.

Wang, M., Isaacman, A., Franz, B. A., & McClain, C. R. (2002). Ocean-color optical property data derived from the Japanese Ocean Color and Temperature Scanner and the French Polarization and Directionality of the Earth's Reflectances: a comparison study. *Applied Optics*, *41*, 974–990.

Wang, M., Liu, X., Tan, L., Jiang, L., Son, S., Shi, W., et al. (2013b). Impacts of VIIRS SDR performance on ocean color products. *Journal of Geophysical Research, [Atmospheres]*, *118*, 10,347–310,360.

Wang, M., & Shi, W. (2006). Cloud masking for ocean color data processing in the coastal regions. *Geoscience and Remote Sensing, IEEE Transactions on*, *44*, 3196-3205.

Wang, M., & Shi, W. (2007). The NIR-SWIR combined atmospheric correction approach for MODIS ocean color data processing. *Optics Express*, *15*, 15722–15733.

Wang, M., & Shi, W. (2009). Detection of ice and mixed ice-water pixels for MODIS ocean color data processing. *Geoscience and Remote Sensing, IEEE Transactions on*, *47*, 2510–2518.

Wang, M., & Shi, W. (2012). Sensor noise effects of the SWIR bands on MODIS-derived ocean color products. *Geoscience and Remote Sensing, IEEE Transactions on*, *50*, 3280–3292.

Wang, M., Shi, W., & Jiang, L. (2012). Atmospheric correction using near-infrared bands for satellite ocean color data processing in the turbid western Pacific region. *Optics Express*, *20*, 741–753.

Wang, M., Shi, W., & Tang, J. (2011). Water property monitoring and assessment for China's inland Lake Taihu from MODIS-Aqua measurements. *Remote Sensing of Environment*, *115*, 841–854.

Wang, M., Son, S., & Shi, W. (2009). Evaluation of MODIS SWIR and NIR-SWIR atmospheric correction algorithms using SeaBASS data. *Remote Sensing of Environment*, *113*, 635–644.

Wang, M., Tang, J., & Shi, W. (2007). MODIS-derived ocean color products along the China east coastal region. *Geophysical Research Letters*, *34*.

Werdell, P. J., & Bailey, S. W. (2005). An improved in-situ bio-optical data set for ocean color algorithm development and satellite data product validation. *Remote Sensing of Environment*, *98*, 122–140.

Werdell, P. J., Bailey, S., Fargion, G., Pietras, C., Knobelspiesse, K., Feldman, G., et al. (2003). Unique data repository facilitates ocean color satellite validation. *EOS, Transactions*, *84*. http://dx.doi.org/10.1029/2003eo380001.